ADVANCED ENERGY MATERIALS
www.advenergymat.de

Thermochemical Oxygen Pumping with Perovskite Reticulated Porous Ceramics for Enhanced Reduction of Ceria in Thermochemical Fuel Production

Mathias Pein, Jens Keller, Christos Agrafiotis, Asmaa Eltayeb, Lena Klaas, Nicole Neumann, Martin Roeb, and Christian Sattler*

Within this work, reticulated monolithic foams and granules made from $CaMnO_{3-\delta}$ and strontium substituted variations are demonstrated to significantly improve the performance of a water splitting redox oxide when employed as a thermochemical oxygen pumping material. Two different process procedures are tested and foams made from $Ca_{0.9}Sr_{0.1}MnO_{3-\delta}$ with a strontium content of 10% outperform all other specimens in both process configurations. Additionally, the performance of $Ca_{1-x}Sr_xMnO_{3-\delta}$ with varying strontium content as a thermochemical oxygen pumping material is studied by means of a newly developed theoretical process model. While the model does not precisely predict the excellent experimental performance of strontium-substitute compositions, it provides valuable insights into the impact of geometry and structure on the specimen's performance in thermochemical oxygen-pumping processes. This work demonstrates the practical application of monolithic 3D structures made entirely from perovskite material in thermochemical oxygen pumping processes and provides a process model that can serve as basis for material screening and process optimization in future work.

1. Introduction

This work focuses on thermochemical oxygen pumping, continuing and expanding the long-term research approach of utilizing porous ceramic structures to implement two-step redox -(reduction-oxidation)-oxide-based thermochemical cycles in applications relevant to Concentrated Solar Power (CSP) plants. The seemingly straightforward[1] chemistry of such a water splitting (WS) and/or carbon dioxide splitting (CDS) cycle for hydrogen and carbon monoxide production, respectively, is described by Equations (1) and (2). Therein, thermal reduction of the oxidized state of an oxide is followed by oxidation of the reduced state via steam or/and carbon dioxide.[2] Two relevant applications sharing the first, common, thermal reduction step are thermochemical storage (TCS) of solar energy and thermochemical oxygen pumping (TCOP). The former is based on the (exothermic) oxidation of the reduced phase of the oxide with air (Equation 3), which can be used off-sun to recover the solar heat stored on-sun during the endothermic reduction reaction.[3] The latter conceives operation of the reduced oxide phase as oxygen sink from a region where oxygen has to be separated or reduced to very low concentration levels and reverse, oxygen source operation of its oxidized state in applications needing oxygen supply. Such oxygen pumping (also known as oxygen chemical scavenging) can be employed for air separation,[4] ammonia production,[5,6] as well as for the performance enhancement of a redox oxide as water/carbon dioxide splitter. By bringing the oxygen-containing effluent from its thermal reduction reaction (Equation 1) in contact with the reduced state of a second redox oxide material, to shift its equilibrium to the right,[7] thus removing the need for mechanical pumping or sweep gassing.[8,9]

$$MeO_x + \Delta H \rightleftharpoons MeO_{x-\delta} + \frac{\delta}{2} O_2 \quad (1)$$

$$MeO_{x-\delta} + \delta H_2O \left(\delta CO_2\right) \rightleftharpoons MeO_x + \delta H_2 \left(\delta CO\right) \quad (2)$$

$$MeO_{x-\delta} + \frac{\delta}{2} O_2 \rightleftharpoons MeO_x + \Delta H \quad (3)$$

Since thermal reduction is favored by high temperatures and low oxygen partial pressures, the cyclic implementation of such schemes is typically performed via a temperature-swing

M. Pein, J. Keller, C. Agrafiotis, A. Eltayeb, L. Klaas, N. Neumann, M. Roeb, C. Sattler
German Aerospace Center (DLR) Institute of Future Fuels
Linder Höhe, 51147 Cologne, Germany
E-mail: mathias.pein@dlr.de
M. Pein, J. Keller, L. Klaas, C. Sattler
RWTH Aachen University Faculty of Mechanical Engineering – Professorship of Solar Fuel Production
52062 Aachen, Germany

The ORCID identification number(s) for the author(s) of this article can be found under https://doi.org/10.1002/aenm.202304454

DOI: 10.1002/aenm.202304454

operation, which can also be substituted or complemented by pressure-swing. The two steps can be implemented at different oxygen partial pressures and at identical or deviating temperature levels (isothermal vs non-isothermal cycles[10]) to influence the driving force and equilibrium state of the reactions. Therefore, the overall implementation in practice is a challenging endeavor,[1] depending on three equally important pillars: a suitable redox oxide material composition, an effective reactor design and an optimized cyclic operation strategy.[11]

Concerning splitting materials, it became evident from very early[12] and was later elaborated via more sophisticated thermodynamics modelling and simulations[6,13–17] that the contradictory thermodynamics with respect to the enthalpy and entropy of reactions (Equations 1 and 2) result in the discouraging fact that the easier the redox pair system material becomes to reduce, the more difficult it is to split H_2O/CO_2 under practical conditions.[1] Oxides that can split H_2O/CO_2within the temperature range of 700–1000 °C require very low oxygen partial pressures to be thermally reduced even at the temperature range of 1300–1600 °C. Such temperature ranges, while generally feasible by CSP tower systems, are very challenging to handle with respect to employed materials and reactor design. Given these temperature levels, it becomes almost compulsory to perform the oxides thermal reduction step at the solar receiver where the required temperatures can be reached. The receiver has to be enhanced to also function as a thermal reduction reactor. The accumulated experience and know-how from the numerous research approaches worldwide has so far converged on performing such cycles below the melting/sublimation point of the redox pair, keeping it in the solid state throughout the process, and operating the material under the so-called non-stoichiometric chemistries, also known as partial redox or oxygen vacancies schemes, to avoid severe lattice structural changes.[18–20] Under this mode, the three state-of-the-art relevant material families, ceria $CeO_{2-\delta}$, ferrites $AFe_2O_{4-\delta}$, and perovskites $ABO_{3-\delta}$, operate in a similar manner (yet under different boundary conditions) and suffer from the same limitations imposed basically by the small width of change in their non-stoichiometry δ,[11] which in turn limits the yield of CO- and H_2-production per cycle. Among them, though, only ferrites- and ceria-based redox pairs have been demonstrated on pilot scale solar reactors, and only ceria has shown excellent stability of both structure and fuel productivity in long-term tests of hundreds of cycles.[21] The "newer" material families explored, perovskites[22,23] and iron aluminate,[24] despite initial encouraging results reported, are still questioned on thermodynamic grounds due to the impractically high excess of oxidant feed streams (water vapor, carbon dioxide) required during their oxidation reaction, which reduces the overall cycle's eventual solar-to-fuel efficiency significantly.[14] Furthermore, they have so far been tested only under small-scale laboratory conditions, with their eventual scalability to ready-for-demonstration solar reactor concepts remaining to be proven.[1] In any case, currently considered materials for redox cycle based WS and CDS require very low oxygen partial pressures during the reduction to reach sufficient round-trip efficiencies of fuel production per cycle. The concept of TCOP has aroused interest in recent years as an energy efficient way to reach the required low oxygen partial pressures in the splitting reactor, potentially outperforming conventional vacuum pumping and inert gas purging.[6,8,25]

Oxides considered for TCS and TCOP are generally waived of the requirement for their reduced state to be capable of H_2O/CO_2 splitting. TCS benefits from high enthalpy of reaction, while TCOP requires high affinity for oxygen at very low oxygen partial pressures. Complete reversibility of the redox reaction and long-term stability are fundamental for both processes. Furthermore, it is possible to explore oxides that can be reduced at lower temperatures or higher oxygen partial pressures (i.e., under air), and with lower energy input as TCS and/or TCOP materials. This logical outcome, on the one hand, affects the quest for proper material compositions and, on the other hand, the type/location of the reactor to be employed: TCS and TCOP do not need to be materialized in solar receiver/reactors, but can be implemented downstream in suitably designed reactors/heat exchangers operating at lower temperatures. Moreover, if employed in a combined or multi-reactor scheme, they can be powered by recovered waste heat from a WS or CDS process that utilizes higher level heat. Taking this rationale one step further, it follows that such applications do not even necessarily need to be coupled to CSP tower facilities, but perhaps can be implemented with high-temperature heat from other sources, e.g. industrial heat from energy-intensive high-temperature industries, such as the cement, glass, ceramics and metal industries.

Addressing the first issue of materials composition, redox pair oxides initially considered and tested for TCS include Co_3O_4/CoO, Cu_2O/CuO, BaO_2/BaO, Mn_2O_3/Mn_3O_4or $(Mn,Fe)_2O_3/(Mn,Fe)_3O_4$,[3,26,27] with Cu_2O/CuO also tested for oxygen pumping;[4,28] none of the reduced states of all these pairs is capable of WS/CDS under practically achievable temperatures. Another commonality is that all these systems operate via the so-called phase change mechanism (i.e., Equation [3] takes place at a specific, unique equilibrium temperature (T_{eq}). Following though the historical trend observed with WS/CDS redox oxides, perovskites were also subsequently considered for both TCS[29,30] and oxygen pumping.[31–34] This attribute is basically due to the versatility of their structure, which can accommodate an enormous variety of metal cations and compositions, hence tuning their properties over a wide range, typically without significant changes in the basic crystal structural motif. A-site substitution of perovskites is a common pathway to optimize material characteristics such as for $Sr_{1-x}Ca_xFeO_{3-\delta}$.[35] For TCS applications, $CaMnO_3$-based perovskite compositions have been identified more suitable[36–38] than their La-based counterparts,[29] which are the preferred ones for WS/CDS[22,39,40] and are also inline with the current ecological and social trends for using low cost and environmentally-benign and non-health-hazardous materials. In contrast to stoichiometric redox pairs, perovskites can be partially reduced, creating oxygen vacancies without severe changes to the crystal structure. This is characterized by a continuous, quasi-linear weight loss/gain during heating/cooling within a wide temperature range.

Regarding reactor design, successful, cyclic, long-term WS/CDS redox operation under solar-irradiation conditions has so far been demonstrated only from reactors employing non-moving porous structures[18,41] like honeycombs[42] or foams manufactured to the highest possible extent out of the redox oxides.[43] Such reactors have been scaled-up to 50 kW by the ETH research group[44] and to 750 kW range by the HYDROSOL project consortium,[45] respectively, with the current versions

of both these reactors employing the redox material as ceramic foams. In the former, single-chamber one currently under testing in a custom-made solar plant at IMDEA, Madrid, Spain, the foams are entirely made out of ceria; the latter, three-reactor system at Plataforma Solar de Almeria[46] is comprised of one reactor consisting entirely of Ni-ferrite coated on ZrO_2foams, one reactor consisting entirely of cerium oxide-coated ZrO_2 foams, and of a third reactor combining foams that are either coated or consist entirely of Ni-ferrite.[47] With respect to their ceramic honeycomb counterparts, ceramic foams exhibit lower pressure drop due to their high degree of interconnectivity, as well as considerable degree of radial mixing, an advantageous feature in processes limited by heat transfer.[48,49]

Along this common TCS/TCOP developmental path, twelve Ca–Mn and Sr–Fe- based perovskite compositions were tested by the authors group with respect to their oxygen release/uptake and corresponding heat effects.[50] $CaMnO_{3-\delta}$ was identified as one of the most efficient oxygen pumping materials in experiments performed with ceria and perovskite powders as the splitting and pumping materials.[51] The authors then proceeded to manufacture porous ceramic foams of diameters 10–15 mm and 20–25 mm entirely made from $CaMnO_3$and the preliminary characterization of the former ones with respect to TCS-relevant attributes.[52] These specimens demonstrated reproducible redox behavior during 46 cycles between 300 and 1100 °C, without any visible deterioration of their structural integrity. Most importantly, comparative dilatometry experiments under the same cyclic conditions with sintered bars of the same material demonstrated a complete recovery of the initial specimen dimensions upon completion of a full heat-up/cooldown redox cycle. Despite an ≈2% expansion upon heating and in contrast to Co_3O_4 and $(Mn,Fe)_2O_3$ redox oxide systems considered for the same application, the initial length was recovered after each cycle. These very positive results concerning the well-known "chemical expansion" issue, i.e., a permanent increase of the structure's dimensions upon repetitive thermal reduction, common to many oxide-based redox systems including ceria[53–55] and cobalt oxide[56] advocate for the introduction of such foams in redox cycling applications. Moreover, it was found that small amounts of *A*-site substitution with Sr benefits structural stability[57] as well as oxidation kinetics.[58]

Following these findings, this work presents an oxygen pumping approach that exploits 3D structures in the form of monolithic $CaMnO_{3-\delta}$, $Ca_{0.95}Sr_{0.05}MnO_{3-\delta}$, and $Ca_{0.9}Sr_{0.1}MnO_{3-\delta}$ perovskite foams, as well as plain granules of these compositions. Experimental results are contextualized with a developed theoretical model, revealing the impact of structural parameters on the oxygen pumping performance.

1.1. Theoretical Considerations

In this work, $CeO_{2-\delta}$ is used as the reference WS and CDS material. Following the thermochemical redox cycle introduced previously, WS can be described as follows:

$$Reduction: CeO_2 + \Delta H \rightleftharpoons CeO_{2-\delta} + \frac{\delta}{2} O_2 \tag{4}$$

$$Oxidation: CeO_{2-\delta} + \delta H_2O \rightleftharpoons CeO_2 + \delta H_2 \tag{5}$$

Therein the reduction reaction is favored when the change in Gibbs free energy $\Delta G = \Delta H - T\Delta S$ of the reaction is below zero until equilibrium is reached at $\Delta G = 0$. Therein, ΔG is strongly influenced by boundary conditions such as temperature or p_{O_2}. The entropy ΔS at non-standard pressures can be described as

$$\Delta S = \Delta S^0 - Rln\left(\frac{p_{O_2}^{0.5}}{p^0}\right) \tag{6}$$

with S^0 as the standard entropy, which can have multiple contributions such as configurational entropy or phonon vibrations and can also depend on the extent of reduction,[59] which is well described by Bulfin et al.[60] and leads to

$$\Delta S^0(\delta) = \delta\left(\frac{1}{2} S_{O_2} + \Delta S_{ph}\right) + \Delta S_{con}(\delta) \tag{7}$$

with $\frac{1}{2}S_{O_2}$ the entropy of oxygen gas, ΔS_{ph} the entropy of vibrational states and $\Delta S_{con}(\delta)$ the configurational entropy. However, the change in enthalpy ΔH^0 can be considered constant for $Ca_{1-x}Sr_xMnO_{3-\delta}$ as was shown by Bulfin et al.[61] The second part of the right side of Equation (4) however is dependent on the partial pressure of oxygen p_{O_2}. ΔG can now be described as

$$\Delta G = \Delta H^0 - T\Delta S^0 + \frac{1}{2} RT\, ln\left(\frac{p_{O_2}}{p^0}\right) \tag{8}$$

with H^0 as the standard enthalpy of reaction. The partial pressure of oxygen impacts the equilibrium of the reaction. Reducing p_{O_2} leads to a larger reduction extent δ at constant temperatures and in turn reduces the equilibrium temperature at constant δ. The reached δ significantly impacts the amount of H_2 produced per thermochemical cycle and thereby the overall efficiency of the process. More so, rewriting Equation (8) with $\Delta G = 0$ at equilibrium, following the approach of Bulfin et al.,[6] as

$$\frac{p_{O_2}}{p^0} = A\, exp\left(\frac{-2\Delta H^0}{RT}\right),\ A = exp\left(\frac{2\Delta S^0}{R}\right) \tag{9}$$

describes the equilibrium p_{O_2} in correlation to the temperature as well as enthalpy and entropy of reaction. A reduced redox oxide can therefore absorb substantial amounts of oxygen at temperatures below the temperature of reduction. This effect is exploited in TCOP to reduce the p_{O_2} in a connected reactor system and drive the reduction reaction therein. While a so-called pumping material (PM) absorbs oxygen until equilibrium according to Equation (9) is reached, the reduction extent of the so-called splitting material (SM) is increased due to the reduced p_{O_2}. TCOP materials can typically be reduced at much lower temperatures, but are not capable of splitting water or carbon dioxide during re-oxidation.

In practice, a TCOP reactor is connected to the main splitting reactor and both are evacuated by conventional vacuum pumping down to pressures below 10 Pa in order to aid with the reduction of the TCOP, but also to allow faster gas diffusion from one reactor to the other. In the described setup, TCOP can be considered as a kind of booster, which has the potential to increase the reduction extent of the employed splitting material without further increasing the reduction temperature or the need to utilize

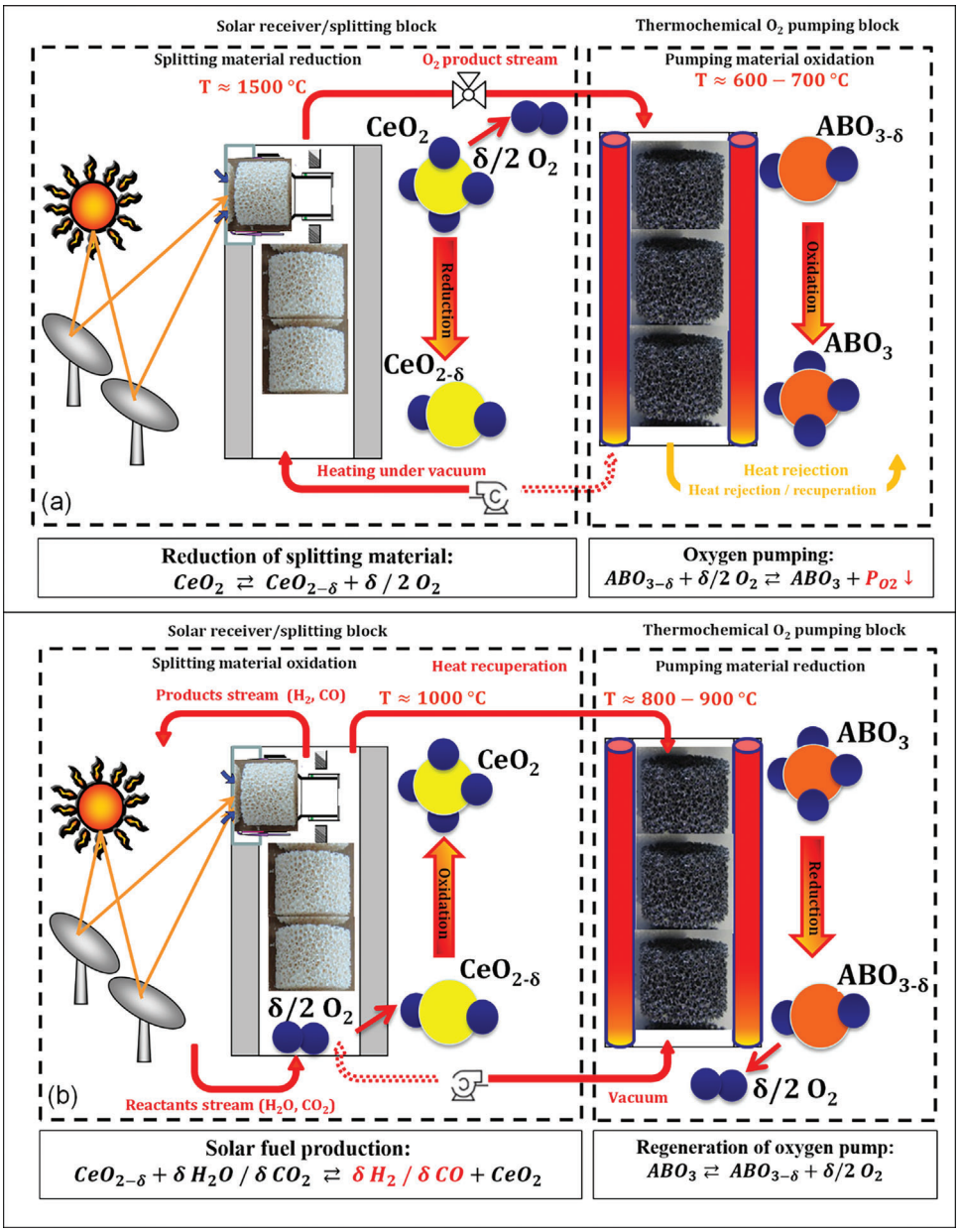

Figure 1. Scheme of concentrated solar energy-driven hydrogen/syngas production aided by thermochemical oxygen pumping with non-moving redox oxide porous structures. a) Reduction of ceria with aid by TCOP b) Oxidation of ceria and recovery of TCOP with recuperated heat. Adapted from Pein et al.[52]

expensive vacuum pumping techniques such as a turbo pump. A schematic illustration of how a practical implementation on a solar tower could be realized, is shown in **Figure 1**.

2. TCOP Methodology

2.1. Experimental

An experimental test rig was used to evaluate the TCOP performance of the investigated perovskite compositions and structures. A schematic illustration of the setup is shown in **Figure 2**.

The test rig was based on previously utilized setups for the demonstration and material screening of TCOP materials.[9,62] Two furnaces were used, one representing the splitting furnace (SF) where the ceria, as the reference material for WS/CDS, is placed, and the other one representing the pumping furnace (PF) containing the TCOP perovskite specimens, respectively. Reference measurements were always carried out without any TCOP specimen present in the PF. Furnaces could be individually evacuated and flushed with a defined mixture of N_2 and O_2 and could be separated or connected through manual valves. The oxygen concentration was determined with an oxygen sensor (MESA GmbH, Lprobe with MK) at the outlet. Mass flows were

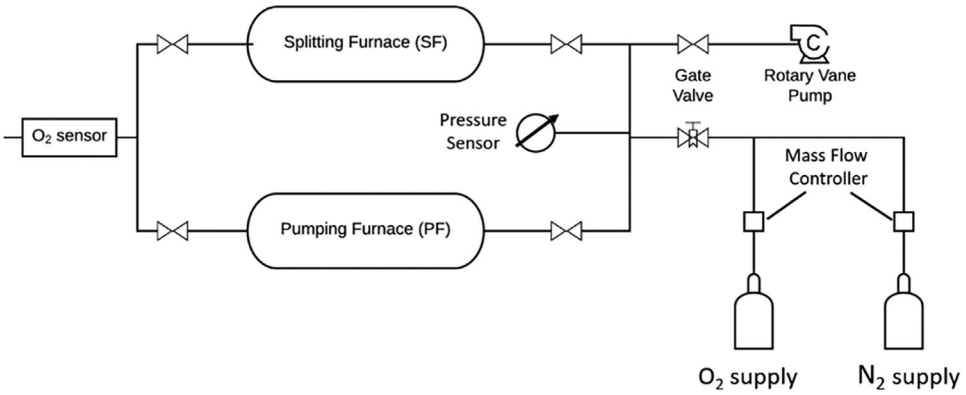

Figure 2. Schematic illustration of used TCOP setup.

individually controlled by MFCs for each gas, and the total mass flow was calibrated to be in the range of 450–460 sccm. In order to reduce the number of variable parameters in this study, reduction and oxidation temperatures were set to T_{red} = 1500 °C and T_{ox} = 1000 °C for the splitting furnace and T_{red} = 800 °C and T_{ox} = 700 °C for the pumping furnace, respectively, in accordance with previously run experiments of the authors group.[62] Two different operational procedures were employed, which can be summarized as simultaneous and separate temperature swing operation, in the following shortly named as "simultaneous case" and "separate case".

In the simultaneous case the temperature swing of the pumping furnace from T_{red} to T_{ox} was performed simultaneously to the temperature swing from T_{ox} to T_{red} in the splitting furnace. In the separate case, the temperature swing in the pumping furnace from T_{red} to T_{ox} was performed while the splitting furnace had already reached T_{red}.

In both cases, the whole setup, which includes both reactors, is evacuated to achieve 10^{-2} mbar right before the temperature swing in the pumping furnace is applied, and the rotary vane pump is detached from the setup at this point. In that sense, the two cases differ with respect to the role that the TCOP sample plays in the reduction of the ceria. In the simultaneous case all oxygen that is released from the ceria during the reduction is absorbed by the TCOP perovskite until equilibrium is reached since the reduction extent of ceria at T_{ox} = 1000 °C and p = 10^{-2} mbar is negligibly small.[9] In contrast, in the separate case the ceria is slightly reduced already at T_{red} = 1500 °C and the TCOP acts as a booster for reduction by absorbing remaining oxygen in the atmosphere, thereby further reducing the p_{O_2} within the setup, shifting the equilibrium toward the reduced state of the ceria. Each measurement was carried out three times, and the results shown in the following are averaged values of these three measurements with the standard deviation as error margin. A detailed description of how $\Delta\delta$ is determined can be found in previously published work by the authors group.[62]

2.2. Theoretical Modelling

The model is based on a 0D-approach to calculate the pressure- and non-stoichiometry evolution over time of PM and SM during the experimental steps. It simulates the experiments carried out in this work by combining the thermodynamics and kinetics of pumping and splitting material with the oxygen transport between both reactors. As the hot zones inside the furnaces are considerably small compared to the total volume of the setup, the gas atmosphere of the whole setup is set to room temperature. This assumption is valid as the main part of the gas atmosphere is located in the tube connection of the furnaces and therefore has a temperature close to room temperature. In contrast, the temperature of the pumping- and splitting material is defined identical to the experimental part of this work.

2.2.1. Modeling framework

In the modeling approach the following experimental steps of the separate and simultaneous case were considered. For each experimental step the volume of each reactor is set to 750 cm^3, which is half of the complete volume of the setup.

Heating up Both Reactors Under Constant Oxygen Partial Pressure: The reactors are underlying isobaric conditions with the surrounding atmosphere during the heating process. The heating time is defined to be 30 min, which is long enough to ensure the material is in an equilibrium state with the surrounding atmosphere after reaching the final temperature. No oxygen-transport between both reactors is considered as both reactors are assumed to have equal pressure. The oxygen partial pressure is set to be 4100 Pa, which is similar to the oxygen partial pressure of experimental step one.

Evacuation of Both Reactors: During the evacuation process no exchange of oxygen between both reactors is assumed to take place as both reactors have equal pressure. The temperature of PM and SM is constant overtime of evacuation. Further the volume of the tube connection to the vacuum pump is neglected.

Heating SM, Cooling PM: The mass transport of oxygen along the tube connection of the reactors due to a pressure difference is considered in the simultaneous and separate case. For each time step the temperature of PM and SM assumed to be constant.

Cooling SM and Flushing with Nitrogen: The cooling process of the splitting material is defined as isochoric. In order to model the experimental procedure, three different approaches were used, depending on the experimental step as described in

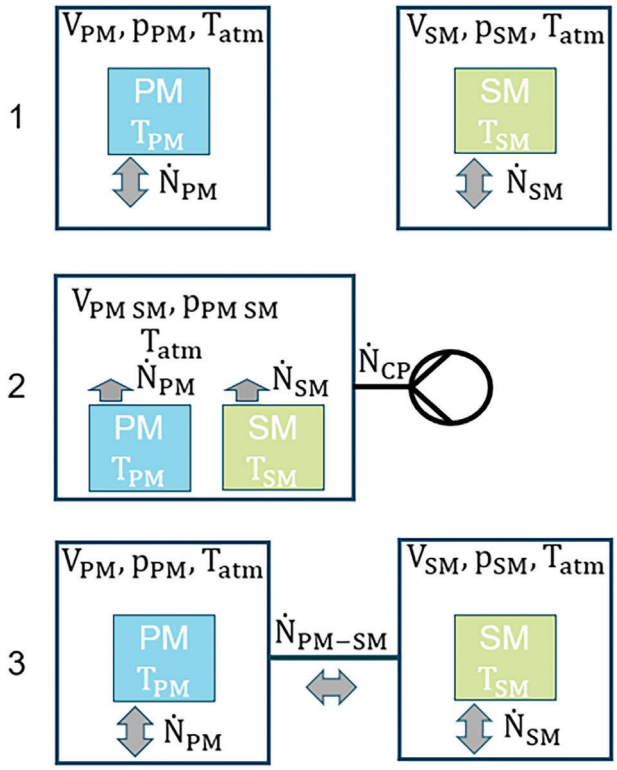

Figure 3. Different modelling approaches according to the experimental steps. V_i and p_i are describing the volume and pressure inside the reactors (SF and PF). T_{atm} describes the temperature of the reactor atmosphere which is set to room temperature. T_i defines the temperature of PM and SM. $\dot{N}_i$ represents the molar flux of oxygen between PM or SM and the reactor atmosphere. $\dot{N}_{CP}$ and $\dot{N}_{PM-SM}$ are representing the molar throughput of the vacuum pump and the molar flux of oxygen between both reactors.

Figure 3. Approach one is used if no mass transport of oxygen between both reactors is considered. This approach is used for modeling the heating up of both reactors as well as for cooling the SM and flushing with Nitrogen. Approach two is used to model the evacuation process. As both reactors will be evacuated in the same time and the pressure in both reactors is assumed to be equal, only the sum of both volumes is considered. Approach three is used for the temperature swing step, in which the mass transport of oxygen along the tube connection is taken into account.

2.2.2. Thermodynamics and Kinetics of Pumping- and Splitting Material

While the splitting- or pumping material (SM/PM) is in a non-equilibrium state with the surrounding atmosphere, the material will constantly react with oxygen available in the surrounding atmosphere until equilibrium is reached. This leads to a change of δ and thus a change of the equilibrium partial pressure as described in Equation (9).

Furthermore, any change in δ of SM or PM influences the $p(O_2)$. If the equilibrium $p(O_2)$ is lower than the $p(O_2)$ of the surrounding atmosphere, the material is oxidized, which leads to a reduction of the $p(O_2)$ in the surrounding atmosphere. A higher equilibrium $p(O_2)$ compared to the $p(O_2)$ of the surrounding atmosphere leads to reduction of the material, causing an increase in the $p(O_2)$ of the surrounding atmosphere.

Equation (10) describes the changed $p(O_2)$ of the reactor atmosphere due to a change of δ. $p_{i,initial}$ is defined as $p(O_2)$ of the reactor atmosphere before a change of δ is occuring. Therein, i indicates the pumping- or splitting material with respect to the ideal gas law:

$$p_i = p_{i,\,initial} + n_i \frac{d\delta_i}{2} \frac{RT_{atm}}{V_i} \tag{10}$$

n_i represents the amount of PM and SM. R defines the ideal gas constant. The exchange of oxygen between the material and the reactor atmosphere will take place until the $p(O_2)$ has reached an equllibrium state as described with the following equation:

$$p_i = p_{O_2}\left(\delta_i + d\delta_i, T_i\right) \tag{11}$$

By inverting to $d\delta$, the molar flux of oxygen with respect to the time step dt can be calculated for the thermodynamic approach.

$$\dot{N}_i = \left(\frac{dn_i}{dt}\right)_{p,T} = \frac{n_i}{2}\left(\frac{d\delta_i}{dt}\right) \tag{12}$$

Regarding the kinetics of the splitting material the derivation of the non-stoichiometry over time of ceria can be calculated by using the following equation:[63]

$$\left(\frac{\partial\delta_{SM}}{\partial t}\right) = \left(0.35 - \delta_{SM}\right)\, k_{Red} - k_{Ox}\delta_{SM}p_{O_2}^{n} \tag{13}$$

k_i describes the kinetic koefficient respectively for the reduction- and oxidation reaction. 0.35 is the maximum non-stoichiometry of SM according to the kinetic approach. The reduction reaction will be infinitesimal slow if the non-stoichiometry approaches the value of 0.35. Due to very fast kinetics of the pumping material during reduction no kinetic equation could be experimentally determined, so the thermodynamic approach will be used. In case of the oxidation process the following equation describes the kinetically derivation of the non-stoichiometry for PM:[64]

$$\left(\frac{\partial\delta_{PM}}{\partial t}\right) = k_0 \exp\left(-\frac{E_A}{k_B T_{PM}}\right)(1-X)^{\beta}\left(\delta_\infty - \delta_0\right) \tag{14}$$

k_0 represents the preexponential factor. E_A describes the activation energy of the oxidation reaction, k_B is defined as the Boltzmann constant. X describes the conversion and β describes a fit-value of this approach. $\delta_\infty$is describing the reduction extend of fully reduced PM and is therefore equal to zero. $\delta_0$is describing the reduction non-stoichiometry at $T_{PM} = 1173$ K and $p_{O_2} = 0.01$ bar. k_0,E_A,β were experimentally determined on granuales with a diameter of 1.25 to 1.6 mm.[58] No such values were available from literature for larger granules and 3D-structures such as the ones investigated within this work.

Furthermore, the change of δ cannot be faster than the limits of the materials' kinetics. Therefore, in each time step the change in δ due to the kinetic approach will be calculated and compared

with the calculated δ of the thermodynamic approach. If the thermodynamic change of $d\delta$ is higher in comparison to the kinetic approach of the material, the reaction is kinetically limited and $d\delta$ will be calculated by the kinetic term. If the reaction is kinetically limited, the thermodynamic approach will be used to calculate $d\delta$. This procedure was carried out for both oxides, ceria and the perovskite PMs, which considered kinetics and thermodynamics in the calculation of $d\delta$ within the process model.

2.3. Gas Transport

The convective mass flow density through a pipe is a function of the pressure difference between both sides of the pipe, the absolute pressure and the temperature of the gas. A simple approach is the Bernoulli-approach where no friction in the gas is considered. The Bernoulli-approach uses the assumption that the pressure difference between both sides of the pipes leads to a force acting on the gas. This force on the other hand leads to acceleration of the gas.[65]

$$A_{Tube}\Delta p_{Tube} = ma \tag{15}$$

A_{Tube} describes the cross-sectional area of the pipe. Δp_{Tube} represents the pressure difference in a given part of the tube. m and a are describing the mass and the acceleration of the gas in this given part of the tube. Under isentropic conditions, solving the Bernoulli-approach leads to the following equation, which describes the molar flux of the gas between both reactors:[65]

$$\dot{N}_{PM-SM} = p_{SM}\sqrt{\frac{2\rho_{SM}}{p_{SM}}}\frac{A_{Tube}}{M_{O_2}}\sqrt{\frac{\kappa}{\kappa-1}\left[\left(\frac{p_{PM}}{p_{SM}}\right)^{\frac{2}{\kappa}}-\left(\frac{p_{PM}}{p_{SM}}\right)^{\frac{1+\kappa}{\kappa}}\right]} \tag{16}$$

ρ_{SM} describes the density of the gas atmosphere in the splitting reactor. M_{O_2} describes the molar weight of oxygen and κ is describing the isentropic exponent for an ideal gas. Due to low heating- and cooling rates and a high diameter of the tube connection, the gas transport is fast in comparison to the change of pressure originating from heating- and cooling the reactors. Thus, the pressure in both reactors is considered to be equal in first approximation during the temperature swing.

2.4. Throughput of the Mechanical Vacuum-Pump

The throughput of the mechanical vacuum-pump is a function of the absolute pressure and can be extracted from the manufacturers datasheet. To calculate the molar flux out of the throughput of the pump, the following equation can be used:[65]

$$\left(\frac{\partial n_{CP}}{\partial t}\right)_{p,T} = \frac{p_{PMSM}}{RT}\frac{1}{\frac{1}{S}+\frac{1}{C}} \tag{17}$$

The tube conductivity C as a function of temperature and pressure can be calculated by the Bernoulli-approach, where p_1 and p_2 describe the pressure on both sides of the tube, respectively the pressure of the reactor atmosphere and the pressure at the inlet of the mechanical vacuum-pump This value can be approximated by the minimum pressure limit of the vacuum pump based on the manufacturers datasheet:[65]

$$C = \frac{RT}{(p_1-p_2)\,M_{O_2}}\sqrt{\frac{2\rho_1}{p_1}}\frac{A}{M_{O_2}}\sqrt{\frac{\kappa}{\kappa-1}\left[\left(\frac{p_2}{p_1}\right)^{\frac{2}{\kappa}}-\left(\frac{p_2}{p_1}\right)^{\frac{1+\kappa}{\kappa}}\right]} \tag{18}$$

Table 1. Used sample weights for perovskite TCOP and ceria as splitting material reference.

Composition	Foam	Granules
$CaMnO_{3-\delta}$	4.29 g	4.26 g
$Ca_{0.95}Sr_{0.05}MnO_{3-\delta}$	4.27 g	4.27 g
$Ca_{0.9}Sr_{0.1}MnO_{3-\delta}$	4.20 g	4.22 g
$CeO_{2-\delta}$		5.02 g

3. Results and Discussion

Granule and foam samples entirely made from the three investigated perovskite compositions $CaMnO_{3-\delta}$ (CMO), $Ca_{0.95}Sr_{0.05}MnO_{3-\delta}$ (CS5MO), and $Ca_{0.9}Sr_{0.1}MnO_{3-\delta}$ (CS10MO) were tested experimentally in a demonstration test rig for TCOP with respect to their capability to decrease the p_{O_2} during reduction of the ceria, thereby increasing the reduction extent δ. Samples were tested in two different process configurations, employing a simultaneous or a separate temperature swing of pumping and splitting material. Sample preparation and testing procedure are described in details in the Experimental Section of this work. Used amounts for the three compositions with two sample types, foam and granules, are given in **Table 1** in the Experimental Section. Exemplary photographs of the employed foam and granules samples are depicted in **Figure 4**.

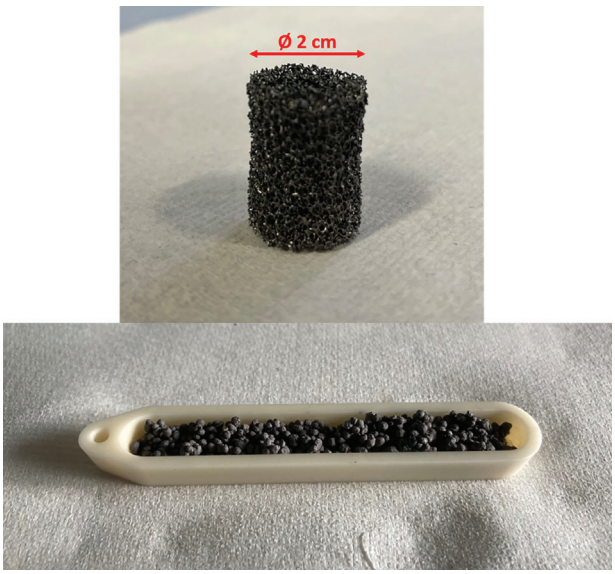

Figure 4. Exemplary samples of a 30 ppi foam (top) and granules (bottom) made from $Ca_{1-x}Sr_xMnO_{3-\delta}$.

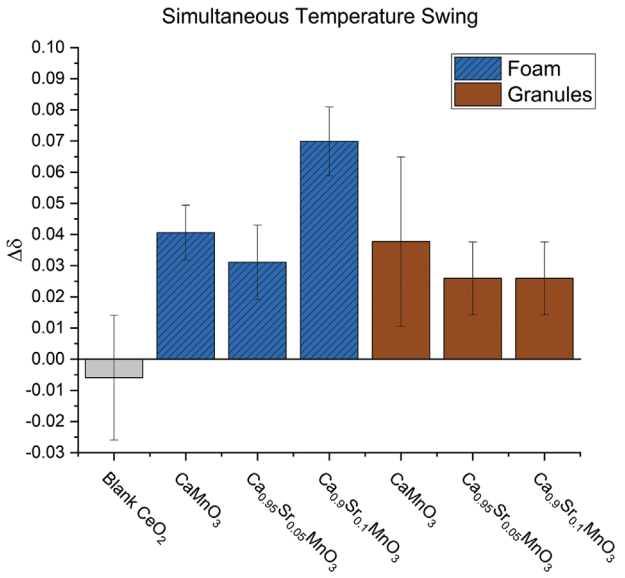

Figure 5. Reached reduction extent $\Delta\delta$ for the reference material ceria with perovskite foams and granules as TCOP in simultaneous temperature swing operation. Reduction and oxidation of ceria carried out at T_{red} = 1500 °C and T_{ox} = 1000 °C respectively.

Experimental results are contextualized by the developed theoretical model and variations between experiment and theory are discussed and analyzed to identify crucial parameters and evaluate potential future use cases of the model.

3.1. TCOP Evaluation

3.1.1. Simultaneous Temperature Swing (Simultaneous Case)

In the simultaneous temperature swing operation, the pumping material acts as an oxygen sink for the oxygen released by the ceria during reduction. While the ceria is only reduced by a negligibly small amount at T_{ox} = 1000 °C during evacuation, the pumping material at T_{red} = 800 °C is already significantly reduced. When the simultaneous temperature swing is applied, the ceria is reduced and releases oxygen, which is in turn absorbed by the pumping material through oxidation. After a short time of equilibration, once the temperature swing was completed, the connection between the two furnaces is closed and no exchange of gas atmosphere is possible. The ceria is cooled down and re-oxidized with a defined gas stream containing 4.1% O_2 diluted in N_2 to analyze the reduction extent reached. A detailed description of the calculation is provided in previous work of the authors group.[51] A total gas flow of 1748 mL min^{-1} was kept constant at all times.

The results of the simultaneous temperature swing tests for foam and granule specimens, plotted as reached reduction extent $\Delta\delta$ of the SM ceria are given in **Figure 5**.

Significant improvement was achieved by the employment of a pumping material. The reduction extent of the blank case is slightly negative, most likely attributable to the experimental error margin rather than thermodynamics. In the absence of a mechanism for oxygen removal during ceria oxidation, all oxygen remains available to the ceria during cool-down causing it to re-oxidize even before the defined re-oxidation gas stream is introduced. Conversely, adding a perovskite pumping material led to reasonable reduction extents of the ceria, by absorbing large amounts of the oxygen released by the ceria during reduction effectively removing it from the atmosphere before cooling down. The largest reduction extent was achieved with $Ca_{0.9}Sr_{0.1}MnO_{3-\delta}$ foam as TCOP sample. The foam specimen outperformed all other samples with a $\Delta\delta$ = 0.07(±0.01). This outperformance was notably compared to the $Ca_{0.9}Sr_{0.1}MnO_{3-\delta}$ granule sample, which achieved $\Delta\delta$ = 0.03(±0.01). However, no clear trends beyond this observation could be discerned.

The higher surface area and shorter diffusion pathways in foams, compared to larger granules, can have a beneficial impact on the kinetics of the oxidation reaction. Larger amounts of oxygen need to be absorbed by the PM in rather short time, increasing the impact of fast oxidation kinetics. While recent results on oxidation kinetics of Sr-doped $CaMnO_{3-\delta}$ in the form of powder and granules by Klaas et al.[64] confirm the positive impact of Sr-content on the oxidation kinetics, ongoing work in the authors group suggests that surface structure and porosity also influence the oxidation kinetics significantly. Latest results correlate higher porosity with potentially faster oxidation kinetics. Investigation of the underlying fundamentals is part of ongoing research.

3.1.2. Separate Temperature Swing

In the separate temperature swing operation, the perovskite TCOP sample can be seen as a "booster" for reduction. While a detailed description of the procedure can be found in the methodology section, a short summary is given here. The two connected furnaces are evacuated to 10^{-2} mbar with ceria at T_{red} = 1500 °C and the perovskite at T_{red} = 800 °C. Due to evacuation, the ceria is already significantly reduced at this point. Then the temperature swing of the TCOP is applied and the perovskite PM absorbs oxygen from the remaining atmosphere in the setup until equilibrium p_{O_2} is reached. In accordance with Equation (9) this reduction of the p_{O_2} causes a shift in equilibrium of the ceria and ultimately leads to further reduction. In that sense, the TCOP is "boosting" the reduction of the ceria by reducing the p_{O_2} during reduction. After the temperature swing of the TCOP is completed, the two furnaces are disconnected and the ceria is cooled down for re-oxidation. Re-oxidation is carried out identical to the previously described simultaneous temperature swing case.

The results given as reached reduction extent $\Delta\delta$ of the SM ceria of the temperature swing tests are depicted in **Figure 6**.

On first sight it can be noted that all tested compositions increase the reduction extent of the reference ceria sample, although the increase is negligible in the case of $CaMnO_{3-\delta}$ granules. Additionally, it can be noted that the error margins were considerably large, which can be explained by the relatively small amount of samples and the nature of how the experiments were carried out – with a lot of manual steps that have to be precisely timed and are prone to some degree of error. Nonetheless the results demonstrate the impact of a TCOP in the context of ceria reduction. Simple reduction of the total pressure to 10^{-2} mbar at the ceria's reduction temperature of 1500 °C led to a reduction extent $\Delta\delta$ = 0.044 (±0.002) in the reference case. Introducing

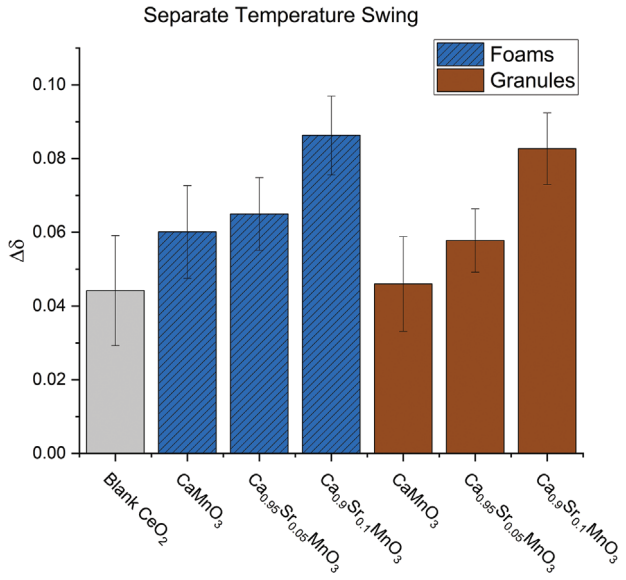

Figure 6. Reached reduction extent $\Delta\delta$ for the reference material ceria with perovskite foams and granules as TCOP in separate temperature swing operation. Reduction and oxidation of Ceria carried out at T_{red} = 1500 °C and T_{ox} = 1000 °C respectively.

$Ca_{1-x}Sr_xMnO_{3-\delta}$ as pumping material increased the $\Delta\delta$, which demonstrated the working principle of a thermochemical oxygen pump. The effect did not appear to be significant for $CaMnO_{3-\delta}$ and $Ca_{0.95}Sr_{0.05}MnO_{3-\delta}$ considering the error margins. However, utilization of $Ca_{0.9}Sr_{0.1}MnO_{3-\delta}$ boosted the reduction extent to remarkable $\Delta\delta = 0.09$ (±0.01) in case of foams and $\Delta\delta = 0.083 \pm (0.004)$ in case of granules respectively.

$Ca_{0.9}Sr_{0.1}MnO_{3-\delta}$ foams, thereby increased the reduction extent in this case by 95%. Taking error margins into account, no significant difference could be observed between foams and granules, although the overall results showed a trend in favor of foams, which is in line with the results of the simultaneous temperature swing case. The same applies for the comparison among the three tested compositions. A trend toward better performance with increasing Sr-content could be observed, which can be explained by the improved kinetics of Sr-doped $CaMnO_{3-\delta}$ and the larger oxygen uptake capacity during the employed temperature swing originating from lower reduction enthalpy. This trend cannot be found in the simultaneous temperature swing case where kinetics are thought to have an even higher impact and surface morphology as well as structure influencing the performance much stronger. Fundamental investigation to identify the underlying mechanisms is part of ongoing research. However, only $Ca_{0.9}Sr_{0.1}MnO_{3-\delta}$ performed significantly better than the other two tested compositions based on the presented results.

The results demonstrate that even under more realistic operating conditions in a bench-top scale demonstration setup, implementing a TCOP to the main reduction step of the ceria can significantly boost the reduction extent and thereby benefit the cyclic efficiency of the thermochemical splitting cycle. $Ca_{0.9}Sr_{0.1}MnO_{3-\delta}$ was found to be the best performing composition in this study. This can be attributed to faster kinetics of the Sr-substituted composition[58] in combination with increased structural stability and suppressed phase transitions due to the lower level of distortion in the crystal lattice.[57] Additionally, foam samples not only hold up to the performance of granule samples, but even outperform them in the simultaneous temperature swing case.

In general, the separate temperature swing case appears to be the more practical operating mode as it allows to heat up the ceria and the TCOP under atmospheric conditions. Evacuation with a mechanical pump down to $p < 1$ mbar is still required in order to increase the reduction of the TCOP material and allow lower p_{O_2} at equilibrium during the splitting materials reduction. Additionally, it ensures fast gas diffusion from one reactor to the other and makes use of the energetically beneficial pressure region of mechanical pumping as shown by Brendelberger et al.[8]

3.2. Theoretical Model

3.2.1. Separate Temperature Swing

The modeling results regarding the evolution of δ over time for the different PM and the blank case are presented in **Figure 7**. The values of reduction extent δ from PM and SM after each experimental step are summarized in **Table 2**.

The curve progression of δ_{PM} has a similar shape for all PM cases, but display an increased level of δ_{PM} with increasing strontium content. This increase can be explained by a lower reaction enthalpy and resulting lower oxygen affinity with higher strontium content, which leads to a higher reduction extent of the PM after evacuation.[61] Since δ_{SM} is not affected by the use of

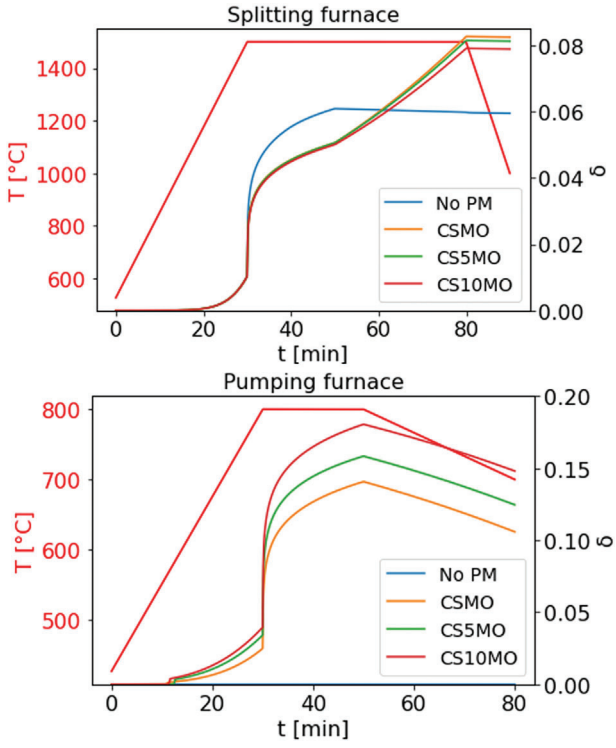

Figure 7. Modeling results for reduction extents δ_{SM} (splitting furnace, top) and δ_{PM} (pumping furnace, bottom) utilizing different pumping materials and the blank (no PM) in the separate temperature swing case.

Table 2. Modeling results of δ_{PM}/δ_{SM} after each step for the different PM. Sep. and Sim. are representing seperate- and simultaneous case.

	Step	$CaMnO_3$		$Ca_{0.95}Sr_{0.05}MnO_3$		$Ca_{0.9}Sr_{0.1}MnO_3$		*No PM*	
		δ_{PM}	δ_{SM}	δ_{PM}	δ_{SM}	δ_{PM}	δ_{SM}	δ_{PM}	δ_{SM}
Sep.	1	0.025	0.010	0.034	0.010	0.040	0.010		0.010
	2	0.141	0.051	0.158	0.051	0.181	0.050		0.061
	3	0.106	0.083	0.125	0.082	0.148	0.079		0.060
	4		0.083		0.081		0.079		0.060
Sim.	1	0.025	0.000	0.034	0.000	0.040	0.000		0.000
	2	0.147	0.000	0.165	0.000	0.187	0.000		0.001
	3	0.079	0.065	0.097	0.064	0.119	0.064		0.025
	4		0.065		0.064		0.064		0.012

a PM for the first two experimental steps, the curve progression is comparable for all PM cases. The main change in δ_{SM} occurs during the evacuation. During the cooling of the sample in step four just a slight change in δ_{SM} is required to adjust the reactor atmosphere to the equilibrium partial pressure.

3.2.2. Simultaneous Temperature Swing

In **Figure 8** the evolution of δ in correlation to the temperatures are presented for the simultaneous temperature swing.

Since the T_{SM} is only 1000 °C during evacuation in step two, δ_{SM} remains negligibly small (close to zero). δ_{PM} rises higher than

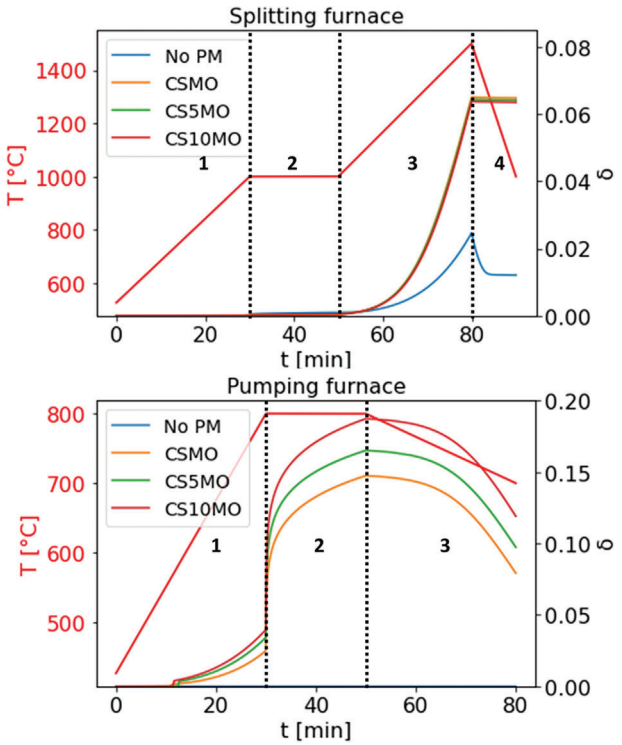

Figure 8. Modeling results for reduction extents δ_{SM} (splitting furnace, top) and δ_{PM} (pumping furnace, bottom) utilizing different pumping materials and the blank (no PM) in the simultaneous temperature swing case.

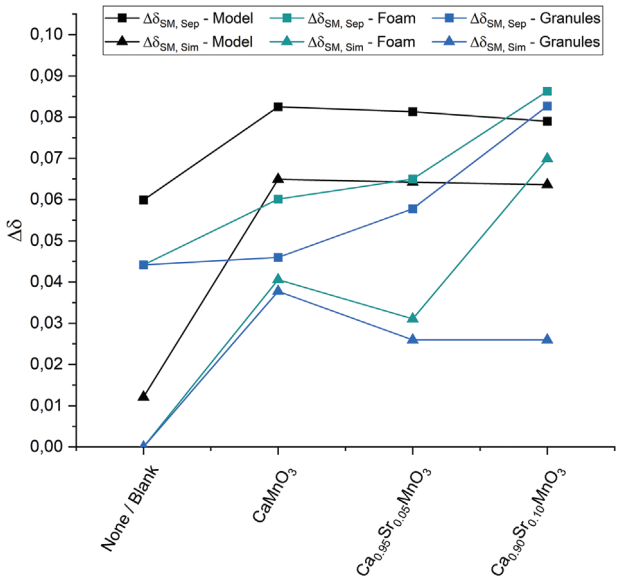

Figure 9. Resulting reduction extent δ_{SM} from the theoretical TCOP model and experiments (foams and granules) for the separate (Sep) and simultaneous (Sim) temperature swing case.

in the separate temperature swing case, which is caused by the reduced $p(O_2)$ in the TCOP setup as the SM only releases very minor amounts of O_2 compared to the separate temperature swing case. However, the general shape of δ_{PM} is very much comparable to the separate temperature swing case, increasing during heat-up and evacuation until the end of step two, and declining due to re-oxidation during step three. In the blank case without a PM, it becomes evident that approximately half of the oxygen released during step three is excluded due to the separation of the furnaces. This leads to a remaining δ_{SM} at the end of step four, which is approximately half of the maximum δ_{SM} at the end of step three for that case.

All values of δ_{SM} and δ_{PM} at the end of each process step as calculated by the TCOP model are summarized in Table 2. δ_{SM} and δ_{PM} after step 4 (before re-oxidation) are also plotted in **Figure 9** together with the experimental values.

It is remarkable that the employment of a pumping material increases the reduction extent δ_{SM} quite significantly in all cases. This general result is in line with the observations made in the experimental part of this work. The highest values of δ_{SM} were obtained for CMO in both cases. In the separate temperature swing case $\delta_{SM} = 0.083$ and in the simultaneous temperature swing case $\delta_{SM} = 0.065$ was obtained, boosting the δ_{SM} by 0.023 and 0.053 respectively. By visualizing all determined δ_{SM} at the end of step 4 in Figure 9, a slight trend can be identified.

The theoretical model predicts better performance for CMO without any Sr-substitution in both cases. Differences in performances with varying Sr-content are minor, yet they are not negligible. In contrast, experiments carried out in this work show that a higher Sr-content in $Ca_{1-x}Sr_xMnO_3$ is beneficial and CS10MO outperforms the other compositions, especially in the separate case. In the simultaneous case, the experimental results of the granules show a similar trend as the model, but for foams again CS10MO exhibits a much better performance compared to

CMO and CS5MO. These results point out that the factors influencing the experimental results cannot all be covered in the theoretical model utilized in this work. For example, macroscopic geometry and resulting permeability as well as surface to bulk ratio and related impacts on reaction kinetics cannot be displayed in the theoretical model, but might play a significant role in the performance of 3D-structures in a process such as TCOP. Moreover, $Ca_{1-x}Sr_xMnO_3$ is well known to undergo phase changes between orthorhombic and cubic when reduced and re-oxidized at high temperatures. This phase change can cause unfavorable kinetics, but is smoothened with increasing Sr-content.[57,62] In line with the argumentation within this work, larger granules suffer much more from the potential phase change than smaller granules as bulk diffusion pathways are smaller and the phase change can be assumed to be fully completed much faster in comparison to larger granules and dense specimens.

Especially phase changes and other structural effects impact the reaction kinetics and are generally of lower impact when diffusion pathways are short and a high surface to bulk ratio is given such as it is the case for foams (wall strength <100 µm) and very small particles and powders. Due to this phase change phenomena, the macroscopic morphology has a significant influence on the performance of the employed PM, which explains why a structural stabilization of Sr-substituted CMO ultimately leads to the observed improved performance of CS10MO and CS5MO over non-substituted CMO. These findings are supported by previous work of the authors, where fine powders were used and CMO outperformed CS10MO under conditions similar to this work.[62] That leads to the conclusion that Sr-substitution of CMO and the induced structural stability is very beneficial when larger 3D-structures and granules are used.

4. Conclusion

The results of this work demonstrate that $Ca_{1-x}Sr_xMnO_3$ structures can be practically implemented as thermochemical oxygen pumping materials and therein act as boosters, which increase the reduction extent of ceria during the reduction reaction. Furthermore, foams have been shown to outperform their granule counterpart, especially in the case of the experimentally best performing material composition $Ca_{0.9}Sr_{0.1}MnO_3$. Two variations of process procedures were tested and both were found to be significantly improved by employing a TCOP material. The relevant reduction extent δ_{SM} was almost doubled in the separate temperature swing case and more than quintupled in the simultaneous temperature swing case.

A process model was developed in order to simulate the experiments based on theoretical considerations and calculated material parameters such as reaction enthalpy and reaction kinetics. Although the general scale of the results is in the expected range of the experimental values, the model predicts a better performance of non-substituted CMO in comparison to Sr-substituted CS5MO and CS10MO, which stays in contrast to the experimental results. The model is based on thermodynamic and kinetic parameters of fine powders available from literature, while experimentally larger granules and 3D-foams have been employed. In such 3D-structures the surface to bulk ratio, macroscopic geometry and also a phase transition of CMO from orthorhombic to cubic at high temperatures and certain reduction extent can have a strong impact on the performance of the different structures and compositions. With further investigation of thermodynamics, kinetics and the impact of structural changes in 3D-structured specimen of the $Ca_{1-x}Sr_xMnO_3$ system and other perovskite compositions, the model can be optimized to better reflect experimental performance of such specimen. Since increasing Sr-substitution is expected to further increase reducibility, but at the cost of oxygen affinity, a wider range of Sr-substitution could be considered to determine limitations of the positive impact of Sr-substitution on the TCOP performance under the given conditions.

In conclusion, the experimental application of 3D-perovskite foam structures as TCOP material was demonstrated to improve the performance of a water-splitting redox oxide such as ceria significantly and even outperform their granule counterparts. The developed process model was shown to properly predict the improved performance by implementing a TCOP and may serve as a powerful tool for material screening in future works. With provision of further information and parameters of reaction kinetics of 3D-structures and the impact of microstructural changes, the model can be optimized toward predicting performance of such structures and compositions in TCOP systems. Moreover, the developed TCOP model allows to vary the process parameters and conditions with ease, which can be exploited to adapt and optimize a TCOP process based on the material of choice. Both of the before mentioned combined will allow for fast screening of materials and process parameters and can help to speed up bringing TCOP with 3D-structured perovskites into application.

Based on the presented work, larger scale experimental demonstration will be possible. The developed process model allows to optimize performance of a TCOP unit and enables fast materials development and process optimization in future works.

5. Experimental Section

Powder Synthesis: Perovskite compositions were prepared by an adjusted solid state synthesis. Stoichiometric amounts of $CaCO_3$ (Merck, Darmstadt, Germany), $SrCO_3$ (Alfa Aesar, Karlsruhe, Germany) and Mn_3O_4 (ERACHEM, Saint-Ghislain, Belgium) powders were dispersed in isopropanol and vigorously stirred for up to 2 h. Powder mixtures were dried for 24 h at 80 °C and fired in alumina crucibles in a Carbolite RHF 14/35 muffle furnace for 24 h at 1200 °C and heating rates of 5 °C min^{-1}. Phase purity after synthesis was confirmed by X-ray diffraction (XRD), performed with a D8 Advance (Bruker, Co-X-ray tube, Lynxe-EyeXET-Detector) in a θ–2θ scan with a step size of 0.02° and 2 s per step.

Foam Preparation: Foam structures were prepared by the well-known replica method resulting in reticulated porous foam structures entirely made from perovskite active material. In order to facilitate the formation of stable slurries and proper dispersion, the synthesized perovskite powders were dry milled for 15 min at 450 rpm utilizing a 1:2 ratio of ∅5 mm ZrO_2 milling balls reaching a narrow particle size distribution with a mean diameter of 5 µm. Using the milled powders, slurries for each composition were prepared identically with a total solid wt.-ratio of 65.4%. 6.6%-wt. of Polyvinylpyrrolidone, PVP K40 (Alfa Aesar, Karlsruhe, Germany), was used as a binder with 3%-wt. of Dolapix CE64 (Zschimmer & Schwarz, Lahnstein, Germany) dispersing agent and de-ionized water. The perovskite powder was first added to the water under stirring, followed by the dispersing agent and the binder. The temperature was raised to 60 °C and the slurries were cooled down after stirring for at least 1 h. Cylindrical polyurethane (PU) foam specimens (FoamPartner, Leverkusen, Germany) of 30 ppi were then dipped into the slurry. Excess slurry was squeezed out and the samples were dried in air over night. The PU foam specimens diameter ranged

from 1.8 to 2.3 cm with a height of 2.3 to 5 cm. Dried samples were then fired in a single stage firing procedure at 1350 °C for 3 h with a heating rate of 1 °C min^{-1} and subsequent cooling with 2 °C min^{-1}. Practically equal weights of the foam and granule specimens were employed.

Granule Preparation: Granulation of perovskite powders was carried out with an EL1 lab-mixer (Gustav Eirich GmbH & Co KG, Germany). Milled powder, identical to the one used for foam production, was mixed with microcrystalline cellulose (MCC) in a 10:3 ratio of perovskite to MCC at 1500 rpm for 10 min. Then the speed was tuned down to 800 rpm and 40 mL of de-ionized water was added. More water was added while stirring drop by drop until the desired particle size and form was reached. Particles were then fired in alumina crucibles in three-stage sintering process. Two debinding stages were employed at 280 and 500 °C for 2 h each, followed by final sintering at 1300 °C for 24 h. A heating rate of 1 °C min^{-1} and a cooling rate of 2 °C min^{-1} was employed. Sintered particles were sieved through a metal sieve stack and particles in the range of 1–5 mm of diameter were used in the TCOP experiments.

Acknowledgements

This work was partly funded by the European Commission, through the HORIZON EUROPE, RIA – Research and Innovation Actions programs HORIZON-CL5-2021-D3-03 under grant agreement No 101084569 and HORIZON-CL5-2022-D4-01-05 under grant agreement No 101104182.

Open access funding enabled and organized by Projekt DEAL.

Conflict of Interest

The authors declare no conflict of interest.

Author Contributions

M.P. performed conceptualization, methodology, investigation, validation, wrote the original draft, and wrote, reviewed, and edited the final manuscript. J.K. performed methodology, validation, wrote the original draft, and wrote, reviewed, and edited the final manuscript. C.A. performed funding acquisition, conceptualization, wrote the original draft, and wrote, reviewed, and edited the final manuscript. L.K. acquired resources, wrote, reviewed, and edited the final manuscript. A.E. acquired resources, wrote, reviewed, and edited the final manuscript. N.N. acquired resources, wrote, reviewed, and edited the final manuscript. M.R. acquired resources, funding acquisition, supervision, and wrote, reviewed, and edited the final manuscript. C.S. acquired resources, funding acquisition, supervision, and wrote, reviewed, and edited the final manuscript.

Data Availability Statement

The data that support the findings of this study are available from the corresponding author upon reasonable request.

Keywords

calcium manganite, ceramic foams, ceria, perovskites, process model, redox oxides, reticulated porous ceramics, thermochemical cycles, thermochemical oxygen pumping

Received: December 22, 2023
Revised: February 27, 2024
Published online: March 29, 2024

[1] A. H. McDaniel, *Curr Opin Green Sustain Chem* **2017**, *4*, 37.
[2] W. C. Chueh, C. Falter, M. Abbott, D. Scipio, P. Furler, S. M. Haile, A. Steinfeld, *Science* **2010**, *330*, 1797.
[3] Project Staff General Atomics, Thermochemical heat storage for concentrated solar power, IEEE, United States, Oct. **2011**, https://doi.org/10.2172/1039304.
[4] B. Moghtaderi, *Energy Fuels* **2010**, *24*, 190.
[5] J. Vieten, D. Gubán, M. Roeb, B. Lachmann, S. Richter, C. Sattler, *AIP Conf. Proc.* **2020**, *2303*, 170016.
[6] B. Bulfin, J. Vieten, C. Agrafiotis, M. Roeb, C. Sattler, *J. Mater. Chem. A* **2017**, *5*, 18951.
[7] T. Rager, J. Golczewski, *Zeitschrift fuer Physikalische Chemie* **2005**, *219*, 235.
[8] S. Brendelberger, H. von Storch, B. Bulfin, C. Sattler, *Sol. Energy* **2017**, *141*, 91.
[9] S. Brendelberger, J. Vieten, M. J. Vidyasagar, M. Roeb, C. Sattler, *Sol. Energy* **2018**, *170*, 273.
[10] I. Ermanoski, J. E. Millera, M. D. Allendorf, *Phys. Chem. Chem. Phys.* **2014**, *16*, 8418.
[11] Y. Lu, L. Zhu, C. Agrafiotis, J. Vieten, M. Roeb, C. Sattler, *Prog. Energy Combust. Sci.* **2019**, *75*, 100785.
[12] M. Lundberg, *Int. J. Hydrogen Energy* **1993**, *18*, 369.
[13] S. Li, V M. Wheeler, A. Kumar, M B. Venkataraman, C L. Muhich, Y. Hao, W. Lipinski, *Energy Technol.* **2022**, *10*, 2000925.
[14] C. L. Muhich, S. Blaser, M. C. Hoes, A. Steinfeld, *Int. J. Hydrogen Energy* **2018**, *43*, 18814.
[15] C. L. Muhich, B. D. Ehrhart, I. Al-Shankiti, B. J. Ward, C. B. Musgrave, A. W. Weimer, *Wiley Interdiscip. Rev.: Energy Environ.* **2016**, *5*, 261.
[16] J. E. Miller, A. H. McDaniel, M. D. Allendorf, *Adv. Energy Mater.* **2014**, *4*, 1300469.
[17] A. Bayon, A. de la Calle, E. B. Stechel, C. Muhich, *Energy Technol.* **2022**, *10*, 2100222.
[18] C. Agrafiotis, M. Roeb, C. Sattler, *Renew Sustain. Energy Rev.* **2015**, *42*, 254.
[19] E. Koepf, I. Alxneit, C. Wieckert, A. Meier, *Appl. Energy* **2017**, *188*, 620.
[20] W. C. Chueh, S. M. Haile, *ChemSusChem* **2009**, *2*, 735.
[21] D. Marxer, P. Furler, M. Takacs, A. Steinfeld, *Energy Environ. Sci.* **2017**, *10*, 1142.
[22] J. R. Scheffe, D. Weibel, A. Steinfeld, *Energy Fuels* **2013**, *27*, 4250.
[23] M. Kubicek, A. H. Bork, J. L. Rupp, *J. Mater. Chem. A* **2017**, *5*, 11983.
[24] A. L. Hoskins, S. L. Millican, C. E. Czernik, I. Alshankiti, J. C. Netter, T. J. Wendelin, C. B. Musgrave, A. W. Weimer, *Appl. Energy* **2019**, *249*, 368.
[25] B. Bulfin, J. Lapp, S. Richter, D. Gubàn, J. Vieten, S. Brendelberger, M. Roeb, C. Sattler, *Chem. Eng. Sci.* **2019**, *203*, 68.
[26] A. J. Carrillo, D. P. Serrano, P. Pizarro, J. M. Coronado, *ChemSusChem* **2015**, *8*, 1947.
[27] A. J. Carrillo, J. González-Aguilar, M. Romero, J. M. Coronado, *Chem. Rev.* **2019**, *119*, 4777.
[28] M. Hänchen, A. Stiel, Z. R. Jovanovic, A. Steinfeld, *Ind. Eng. Chem. Res.* **2012**, *51*, 7013.
[29] S. M. Babiniec, E. N. Coker, J. E. Miller, A. Ambrosini, *Sol. Energy* **2015**, *118*, 451.
[30] Z. Zhang, L. Andre, S. Abanades, *Sol. Energy* **2016**, *134*, 494.
[31] J. Vieten, B. Bulfin, F. Call, M. Lange, M. Schmücker, A. Francke, M. Roeb, C. Sattler, *J. Mater. Chem. A* **2016**, *4*, 13652.
[32] J. Vieten, B. Bulfin, D. E. Starr, A. Hariki, F. M. F. de Groot, A. Azarpira, C. Zachäus, M. Hävecker, K. Skorupska, N. Knoblauch, M. Schmücker, M. Roeb, C. Sattler, *Energy Technol.* **2019**, *7*, 131.
[33] M. Ezbiri, A. Reinhart, B. Huber, K. M. Allen, A. Steinfeld, B. Bulfin, R. Michalsky, *React. Chem. Eng.* **2020**, *5*, 685.
[34] M. Ezbiri, K. M. Allen, M. E. Gàlvez, R. Michalsky, A. Steinfeld, *ChemSusChem* **2015**, *8*, 1966.
[35] T. Jia, E. J. Popczun, J. W. Lekse, Y. Duan, *Appl. Energy* **2021**, *281*, 116040.

[36] S. M. Babiniec, E. N. Coker, J. E. Miller, A. Ambrosini, *Int. J. Energy Res.* **2016**, *40*, 280.
[37] L. Imponenti, K. J. Albrecht, R. Kharait, M. D. Sanders, G. S. Jackson, *Appl. Energy* **2018**, *230*, 1.
[38] L. Imponenti, K. J. Albrecht, J. W. Wands, M. D. Sanders, G. S. Jackson, *Sol. Energy* **2017**, *151*, 1.
[39] A. H. McDaniel, E. C. Miller, D. Arifin, A. Ambrosini, E. N. Coker, R. O'Hayre, W. C. Chueh, J. Tong, *Energy Environ. Sci.* **2013**, *6*, 2424.
[40] J. Vieten, B. Bulfin, P. Huck, M. Horton, D. Guban, L. Zhu, Y. Lu, K. A. Persson, M. Roeb, C. Sattler, *Energy Environ. Sci.* **2019**, *12*, 1369.
[41] C. Agrafiotis, M. Roeb, C. Sattler, in *Comprehensive Energy Systems* (Ed.: I. Dincer), Volume 4, Elsevier, USA **2018**, pp. 733–761.
[42] M. Roeb, J.-P. Säck, P. Rietbrock, C. Prahl, H. Schreiber, M. Neises, L. de Oliveira, D. Graf, M. Ebert, W. Reinalter, M. Meyer-Grünefeldt, C. Sattler, A. Lopez, A. Vidal, A. Elsberg, P. Stobbe, D. Jones, A. Steele, S. Lorentzou, C. Pagkoura, A. Zygogianni, C. Agrafiotis, A. G. Konstandopoulos, *Sol. Energy* **2011**, *85*, 634.
[43] P. Furler, J. Scheffe, D. Marxer, M. Gorbar, A. Bonk, U. Vogt, A. Steinfeld, *Phys. Chem. Chem. Phys.* **2014**, *16*, 10503.
[44] E. Koepf, S. Zoller, S. Luque, M. Thelen, S. Brendelberger, J. González-Aguilar, M. Romero, A. Steinfeld, *AIP Conf. Proc.* **2019**, *2126*, 180012.
[45] J.-P. Säck, S. Breuer, P. Cotelli, A. Houaijia, M. Lange, M. Wullenkord, C. Spenke, M. Roeb, C. Sattler, *Sol. Energy* **2016**, *135*, 232.
[46] A. González-Pardo, T. Denk, A. Vidal, *AIP Conf. Proc.* **2018**, *2033*, 130007.
[47] S. Lorentzou, A. Zygogianni, C. Pagkoura, G. Karagiannakis, A. G. Konstandopoulos, J. P. Saeck, S. Breuer, M. Lange, J. Lapp, T. Fend, M. Roeb, A. J. Gonzalez, A. V. Delgado, J. P. Brouwer, R. C. Makkus, S. J. Kiartzis, *AIP Conf. Proc.* **2018**, *2033*, 130010.
[48] M. V. Twigg, J. T. Richardson, *Ind. Eng. Chem. Res.* **2007**, *46*, 4166.
[49] M. Twigg, J. Richardson, *Chem. Eng. Res. Des.* **2002**, *80*, 183.
[50] C. Agrafiotis, M. Pein, D. Giasafaki, S. Tescari, M. Roeb, C. Sattler, *J. Sol. Energy Eng.* **2019**, *141*, 021010.
[51] M. Pein, C. Agrafiotis, J. Vieten, D. Giasafaki, S. Brendelberger, M. Roeb, C. Sattler, *Sol. Energy* **2020**, *198*, 612.
[52] M. Pein, L. Matzel, L. de Oliveira, G. Alkan, A. Francke, P. Mechnich, C. Agrafiotis, M. Roeb, C. Sattler, *Adv. Energy Mater.* **2022**, *12*, 2102882.
[53] A. Atkinson, T. Ramos, *Solid State Ionics* **2000**, *129*, 259.
[54] N. Knoblauch, H. Simon, M. Schmücker, *Solid State Ionics* **2017**, *301*, 43.
[55] C. L. Muhich, *J. Phys. Chem. C* **2017**, *121*, 8052.
[56] C. Agrafiotis, S. Tescari, M. Roeb, M. Schmücker, C. Sattler, *Sol. Energy* **2015**, *114*, 459.
[57] L. Klaas, M. Pein, P. Mechnich, A. Francke, D. Giasafaki, D. Kriechbaumer, C. Agrafiotis, M. Roeb, C. Sattler, *Phys. Chem. Chem. Phys.* **2022**, *24*, 27976.
[58] L. Klaas, B. Bulfin, D. Kriechbaumer, M. Roeb, C. Sattler, *Phys. Chem. Chem. Phys.* **2023**, *25*, 9188.
[59] R. J. Panlener, R. N. Blumenthal, J. E. Garnier, *J. Phys. Chem. Solids* **1975**, *36*, 1213.
[60] B. Bulfin, J. Vieten, C. Agrafiotis, M. Roeb, C. Sattler, *J. Mater. Chem. A* **2017**, *5*, 18951.
[61] B. Bulfin, J. Vieten, D. E. Starr, A. Azarpira, C. Zachäus, M. Hävecker, K. Skorupska, M. Schmücker, M. Roeb, C. Sattler, *J. Mater. Chem. A* **2017**, *5*, 7912.
[62] M. Pein, C. Agrafiotis, J. Vieten, D. Giasafaki, S. Brendelberger, M. Roeb, C. Sattler, *Sol. Energy* **2020**, *198*, 612.
[63] B. Bulfin, A. J. Lowe, K. A. Keogh, B. E. Murphy, O. Lübben, S. A. Krasnikov, I. V. Shvets, *J. Phys. Chem. C* **2013**, *117*, 24129.
[64] L. Klaas, B. Bulfin, D. Kriechbaumer, M. Roeb, C. Sattler, *Phys. Chem. Chem. Phy.: PCCP* **2023**, *25*, 9188.
[65] W. Jitschin, *Strömung von Gasen Wutz Handbuch Vakuumtechnik* (Ed.: K. Jousten), Vieweg+Teubner Verlag, Wiesbaden **2004**, https://doi.org/10.1007/978-3-322-96971-2_4.